Crystalline structure and magnetic behavior of the $Ni_{41}Mn_{39}In_{12}Co_8$ alloy demonstrating giant magnetocaloric effect

2016 Smart Mater. Struct. 25 085013

(http://iopscience.iop.org/0964-1726/25/8/085013)

IOP Publishing Smart Materials and Structures
Smart Mater. Struct. **25** (2016) 085013 (8pp) doi:10.1088/0964-1726/25/8/085013

Crystalline structure and magnetic behavior of the $Ni_{41}Mn_{39}In_{12}Co_8$ alloy demonstrating giant magnetocaloric effect

A S B Madiligama[1], P Ari-Gur[2], V G Shavrov[3], V V Koledov[3], S Calder[4], A V Mashirov[3], A P Kamantsev[3], E T Dilmieva[3], L Gonzalez-Legarreta[5], B H Grande[5], V V Vega[5] and A Kayani[1]

[1] Department of Physics, Western Michigan University, Kalamazoo, MI 49008-5252, USA
[2] Mechanical and Aerospace Engineering, Western Michigan University, Kalamazoo, MI 49008-5343, USA
[3] Kotelnikov Institute of Radio-engineering and Electronics of RAS, Moscow, 125009, Russia
[4] Oak Ridge National Laboratory, Bethel Valley Rd, 37831, Oak Ridge, TN, USA
[5] Department of Physics, University of Oviedo, E-33007, Oviedo, Spain

E-mail: amila.bandara@wmich.edu

Received 23 March 2016, revised 21 June 2016
Accepted for publication 27 June 2016
Published 19 July 2016

Abstract

Magnetic cooling is a green cooling technology, which is more energy efficient than existing fluid-compression cooling machines. $Ni_{41}Mn_{39}In_{12}Co_8$ alloy, which demonstrates promising magnetocaloric performances, was investigated using neutron diffraction and thermomagnetic measurements. The austenite structure is cubic $L2_1$ ($Fm\bar{3}m$), while that of the martensite is a mix of 8 and 6 M modulated monoclinic structures ($P\,1\,2/m\,1$). The austenitic site occupancy refinements reveal that all substituting Co atoms occupy Ni-sites. Most Mn atoms (65%) are in the Mn-sites and the rest go to In-sites (about 35%) and Ni-sites (less than 5%). This disorder of the magnetic atoms (Mn, Ni and Co) in the austenitic phase remains unchanged during the martensitic transition. The distortions of the interatomic distances due to the modulation of the martensitic structures further enhance the disorder in the magnetic interactions. Thermomagnetic measurements indicate that the austenitic phase is ferromagnetic. Cooling to below 250 K, where the alloy loses its ferromagnetic nature, and down to 50 K, the lack of any antiferromagnetic Bragg peaks suggests no antiferromagnetic ordering in the martensitic phase. At very low temperatures in the martensitic phase, spin glass magnetic nature is identified by magnetic measurements, and the spin-glass transition temperature is ~19 K.

Keywords: giant magnetocaloric effect, Heusler alloys, spin-glass, 6 M and 8 M modulated martensite

(Some figures may appear in colour only in the online journal)

1. Introduction

Ni–Mn–X (X = In, Ga, Sn, and Sb) alloys exhibit unique multifunctional properties associated with their magnetic field-induced metamagnetic phase transitions. Magnetic shape memory [1], magnetic superelasticity [2], giant magnetocaloric [3] and giant solid-state barocaloric effects [4] are some of the phenomena, which make these alloys important in many technological applications. Some of these alloys exhibit giant magnetocaloric effect (GMCE) associated with the magnetic field-induced first-order phase transitions around room temperature. That makes them highly promising as refrigerants for near room temperature-cooling systems [5–7]. When compared to other giant magnetocaloric materials, Ni–Mn–In based alloys have a number of advantages, such as, lower cost, eco-friendlier, better oxidation resistance, and

Table 1. Summary of the RBS analysis.

Position	Energy of the O^{+4} ion beam (MeV)	Incident/scattering angle (°)	Calculated elemental composition (%)			
			Ni	Mn	In	Co
1	15	0/150	40.68 ± 0.30	39.22 ± 0.23	11.60 ± 0.12	8.50 ± 0.65
2	15	0/150	40.70 ± 0.15	39.10 ± 0.16	11.60 ± 0.16	8.60 ± 0.51

higher strength [5]. Substitution of a small percentage of cobalt in Ni–Mn–In alloys enhances their magnetocaloric performance significantly [5]. Additionally, by controlling the amount of cobalt, the martensitic transition temperature (T_M) can be manipulated [8]. All these desirable properties of Ni–Mn–In–Co Heusler alloys make them potential candidates for magnetic cooling refrigerants.

An application of a magnetic field at a certain temperature range in some Ni–Mn–In–Co alloys will cause the martensitic phase to transform into an austenitic phase; the temperature range and strength of the required field depend on the composition. The main contribution of the observed GMCE in these alloys is associated with structural phase transition. Usually, the magnetic entropy contribution from spin alignment is relatively small, but vital as the driving force of the magneto-structural transitions [5]. For a wide range of compositions, the cubic $L2_1$ structure [5, 9, 10] and ferromagnetic ordering of the austenitic phase of these alloys are well known [6, 11]. However, depending on the composition, the structure of the martensite has several possibilities. Some reported structures for the martensite include non-modulated face-centered tetragonal ($L1_0$) [9], 5 M modulated orthorhombic [10, 12], 5 M [5, 10], 6 M [9] and 7 M modulated monoclinic [10]. In these modulated structures, the interatomic distance between magnetic atoms vary significantly [11]. This causes different magnetic interactions between magnetic moments. Additionally, the randomness of the site occupation of strongly magnetic Mn atoms in non-stoichiometric alloys may result in different magnetic configurations in the martensitic phase, such as antiferromagnetic ordering [13] and disordered spin-glass (in much lower temperatures below the martensitic transition) [11, 14].

This study is devoted to the investigation of the crystalline structure and magnetic states of the both austenitic and martensitic phases of a potential magnetocaloric Ni–Mn–In–Co alloy. This alloy exhibits promising magnetocaloric performances to be considered as a potential solid-state magnetic refrigerant. Calculations based on Maxwell relation, show that the maximum entropy change in this alloy, is 13 J kg^{-1} K^{-1} at 310 K under an applied magnetic field of 3 T [6]. The understanding of the behavior of the phase fractions of the austenitic and martensitic phases with temperature is also a major goal of this research.

2. Sample preparation and experimental techniques

A polycrystalline sample of the $Ni_{41}Mn_{39}In_{12}Co_8$ alloy was prepared by the arc-melting method under an argon atmosphere, and the sample was tested in the as-cast state. The chemical composition of the alloy was determined by the Rutherford Backscattering Spectrometry (RBS) technique carried out in the 6 MV Tandem Van de Graaff accelerator laboratory at Western Michigan University [15]. The projectile ion type (O^{+4}), the energy of the ion beam (15 MeV), and the scattering angle (150°) were selected for maximum resolution between backscattered ions by Ni and Co atoms, which have similar atomic masses. Data were analyzed to determine the depth profile composition of the alloys using SIMNRA [16]. Neutron diffraction measurements of the alloy were conducted at the constant wavelength (0.15374 nm) neutron powder diffractometer, HB2A, at Oak Ridge National Laboratory [17]. Data were collected at different temperatures in the range from 50 to 600 K. Rietveld refinements of neutron diffraction data were done using general structure analysis system (GSAS) [18] and GSAS EXPGUI [19]. The refined crystalline structures were drawn by DRAWxtl [20]. Thermomagnetization measurements of the alloy with zero-field cooling (ZFC), field-cooling (FC), and field-heating routines were carried out between 50 and 400 K, and under four different magnetic fields using a vibrating sample magnetometer. In addition, thermomagnetic measurements of the alloy in the temperature range 1.9–100 K were collected using SQUID magnetometer at the University of Michigan.

3. Results and discussion

3.1. Chemical composition and site occupancies

Magnetic and magnetocaloric properties of Ni–Mn–X based Heusler alloys are strongly dependent on the chemical composition. Therefore, the chemical composition of the alloy needs to be determined as accurately as possible. RBS data of the alloy on two positions of the sample surface were collected to get a better accuracy for the chemical composition. Summary of the RBS data analysis is given in table 1. The composition of the alloy as determined by the RBS technique is $Ni_{41}Mn_{39}In_{12}Co_8$.

A critical aspect of this experiment was the determination of site occupancies of all atoms in order to calculate the chemical order in the alloy. In the austenitic cubic $L2_1$ structure, there are three different crystallographic sites: Mn (4a), In (4b), and Ni (8c). In the site occupancy refinements, it was assumed that all three crystallographic sites can potentially be occupied by any of the four atoms. Compared to the synchrotron diffraction technique, neutron diffraction is a

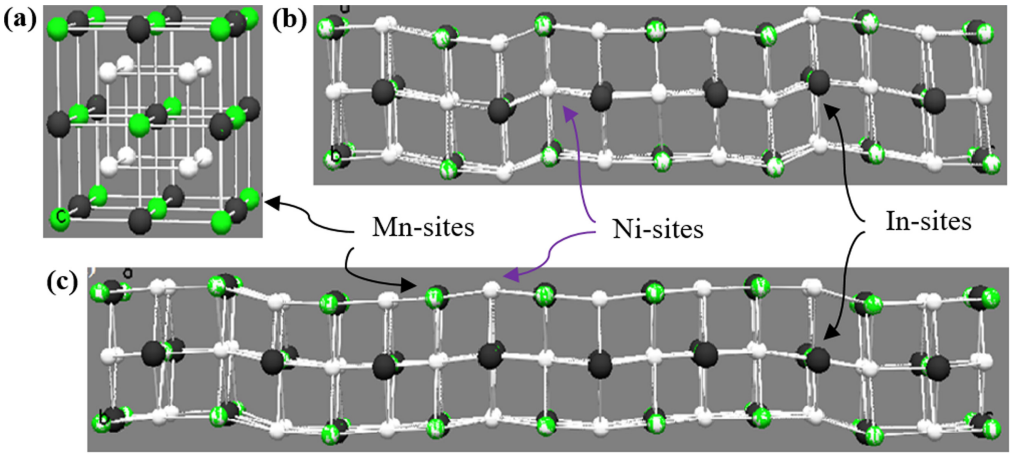

Figure 1. Schematic diagrams (generated by the DRAWxtl software [20]) of the crystalline structures of $Ni_{41}Mn_{39}In_{12}Co_8$ alloy based on refinements of the neutron diffraction data. (a) The austenitic $L2_1$ cubic crystalline structure at 400 K. This one belongs to $Fm\bar{3}m$ space group. (b) 6 M modulated and (c) 8 M modulated martensitic phases at 250 K; both belong to the $P\,1\,2/m\,1$ monoclinic space group.

Table 2. Summary of the site occupancy refinement in the austenitic phase.

Element		Ni	Mn	In	Co
Occupation of Wyckoff positions (%)	4a (4 atoms per unit cell)	4.23 ± 0.07	95.77 ± 0.07	0	0
	4b (4 atoms per unit cell)	0	53.37 ± 0.48	46.67 ± 0.06	0
	8c (8 atoms per unit cell)	79.11 ± 0.03	4.11 ± 0.04	0	16.78 ± 0.01
Composition (%)		40.59 ± 0.05	39.29 ± 0.06	11.75 ± 0.02	8.37 ± 0.01

better tool to determine the site occupancies of these atoms. The scattering amplitudes of the constituent atoms (Ni, Mn, Co, and In) for neutrons are significantly different (bound scattering lengths of Ni, Mn, Co, and In are 10.3, −3.73, 2.49, and 4.01 fm respectively) [21]. The chemical order of the alloy was calculated by the site-occupancy refinements of its neutron diffraction data collected at three different temperatures (600, 450 and 400 K) in the austenitic phase. It was found that ~97% of the Co atoms occupy Ni-sites and the rest occupy the Mn-sites. This result is very similar to the formation energy calculations of the austenitic structure of Ni–Mn–Ga alloys carried out by Bai *et al* [22]. In that study, it was recorded that in Ni–Mn–Ga alloys, the substituted Co occupies the regular Ni-sites. The preference of Co atoms to occupy the Ni-site could be explained in terms of the atomic radii of the Ni and Co atoms. Co has the closest atomic radius to Ni compared to the other two elements in this alloy, Mn and In, and hence Co prefers to occupy Ni-sites. The In-site is occupied by both Mn and In atoms; the proportions are about 50% of each In and Mn. Over 60% of the Mn atoms was found in the Mn-sites, about 35% in In-sites, and less than 5% in Ni-sites. Compositions calculated from the refinement of neutron diffraction data are summarized in table 2. It should be noted that even though the values calculated for site occupancies at different temperatures are precise; ideally, these numbers (calculated occupancies) should be the same for each temperature. The composition calculated by the site occupancy results is in agreement with the value calculated by the RBS technique. The final chemical composition was taken to be $Ni_{41}Mn_{39}In_{12}Co_8$.

3.2. Crystalline structures

Crystalline structures at different temperatures in the range from 50 to 600 K were determined by neutron diffraction refinement. The austenitic structure was found to be cubic $L2_1$ (figure 1(a)), which belongs to the $Fm\bar{3}m$ space group. The lattice parameter of the $L2_1$ structure at five different temperatures in the range from 300 to 600 K was also calculated by the refinements. The temperature dependence of the lattice parameter is plotted in figure 2. The lattice parameter increases linearly with increasing temperature. The linear thermal expansion coefficient of this alloy in the 300–600 K range was calculated to be $(9.2056 \pm 0.0043) \times 10^{-6}\,K^{-1}$, which is about 70% of that of pure Ni ($1.44 \times 10^{-5}\,K^{-1}$) [23].

Similar to the constraints used by Righi [24, 25] in the refinement of the modulated structures of the martensitic phase of the Ni_2MnGa alloy, the following steps were taken to reduce the number of parameters in the refinements. First, the modulations of the martensitic structures occur along the [001] direction of the monoclinic unit cell (this corresponds to [110] direction in the austenite). Second, both *x*- and *y*-coordinates of all atoms were allowed to refine, while the *z*-coordinate was kept constant. Third, the amplitude of modulation of every atom in the (001) plane was the same. For the martensitic phase of this alloy, the refinement revealed a mix of 6 M (figure 1(b)) and 8 M (figure 1(c)) modulated monoclinic structures. Lattice parameters of all the crystalline structures in both phases, along with the agreement factors of the respective refinement cycle are summarized in table 3.

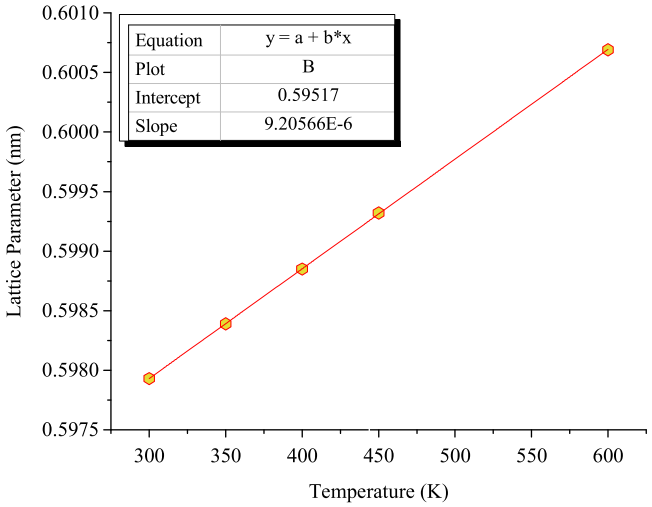

Figure 2. Variation of the lattice parameter of the austenitic structure with the temperature.

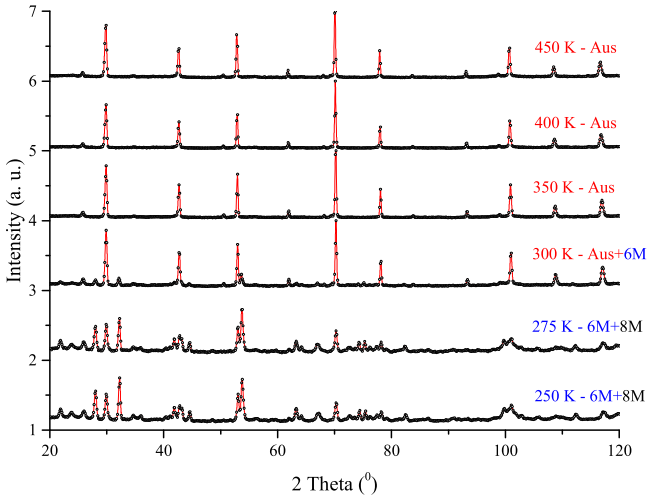

Figure 3. The growing of the austenitic phase (at 450 K alloy is pure austenite) from pure martensitic phases (at 50 K).

The a and b lattice parameters of the two modulated structures are very similar. However, the lattice parameter along the Z-direction, which is the direction of the modulation, is completely different (as expected). The values obtained by dividing the lattice parameter c by the respective modulation of the 6 M and 8 M structures are 0.433 and 0.411 nm, respectively. The stacking sequences along the Z-direction are $2\bar{2}1\bar{4}2\bar{2}$ for 6 M and $2\bar{1}4\bar{2}4\bar{1}2$ for 8 M modulated structures.

3.3. Phase fraction analysis

The evolving of the austenitic phase (at 450 K) from pure martensitic phases (at 250 K) is demonstrated in figure 3. The diminishing of the martensitic Bragg peaks and the growing of the austenitic Bragg peaks can be observed as the temperature is increasing from 250 to 450 K. In order to determine the contribution of each phase to the total diffraction pattern, the phase fractions at different temperatures in the range from 50 to 600 K were calculated by neutron diffraction refinements. From those phase fraction values of each phase (S_i), the weight fractions of each phase (W_i) were calculated using equation (1)

$$W_i = (S_i M_i V_i) \Big/ \left(\sum_j S_j M_j V_j \right), \tag{1}$$

where M_i and V_i are the unit cell mass and volume, respectively. The unit cell volumes were determined by the lattice parameters of the crystalline unit cells of the relevant phases.

The variation of weight fractions of the phases with the temperature is given in figure 4. The entire temperature range can be classified into three main regions. In the first region, between 600 and 350 K, the alloy is a single-phase austenite. The agreement between the experimental and calculated diffraction patterns at 600 K is given in the figure 5. All the observed Bragg peaks belong to the cubic $L2_1$ structure and with no trace of the martensitic phase.

In the second region (i.e. from 350 to 270 K), three phases, austenitic, 6, and 8 M martensitic phases co-exist. The experimental and the calulated diffraction patterns at 300 K

Table 3. Agreement factors of the Rietveld refinements and lattice parameters of the three phases.

		Lattice parameters				[a]Agreement factors		
T (K)	Phase(s)	a (nm)	b (nm)	c (nm)	β (°) ($\alpha = \gamma = 90^0$)	R_w [b]	R_p [c]	χ^2 [d]
600	Aus	0.601	—	—	90	4.8	3.5	3.0
300	Aus/6 M	0.598/0.441	0.598/0.556	0.598/2.592	90/93.69	3.4	2.7	1.6
250	6 M/8 M	0.440/0.443	0.554/0.558	2.582/3.288	93.65/91.05	1.9	1.4	1.2

[a] Agreement factors of the Rietveld refinements are defined as [18].
[b] $R_P = 100 \sum |I_0 - I_C| / \sum I_0$.
[c] $R_{WP} = 100 \sqrt{\left(\sum w_i (I_0 - I_C)^2 / w_i I_0^2 \right)}$.
[d] $\chi^2 = \sum w_i (I_0 - I_C)^2 / (N_{obs} - N_{var})$.
where,
I_0 and I_C are the observed and calculated diffraction intensities,
w_i is the weight assigned to each intensity,
N_{obs} and N_{var} are the total number of observations and the number of variables in the least square refinement, respectively and
χ^2 is the goodness of the fit.

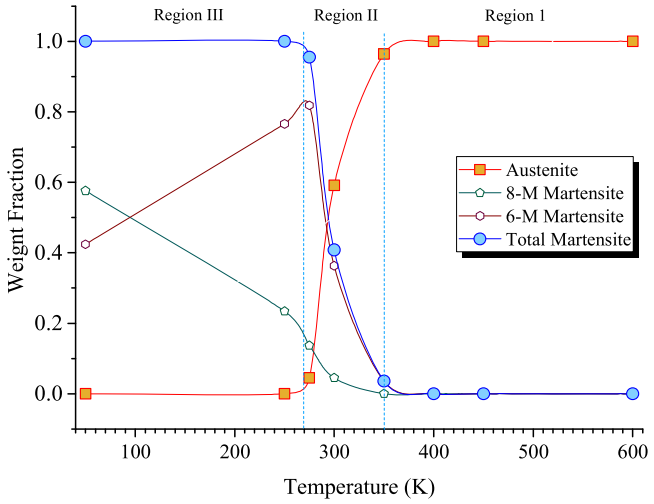

Figure 4. Variation of the phase fractions of the austenite, total martensite, 6, and 8 M martensitic phases with the temperature (50–600 K). The phase fraction of the 6 M phase is higher than that of the 8 M phase in all the studied temperatures except 50 K.

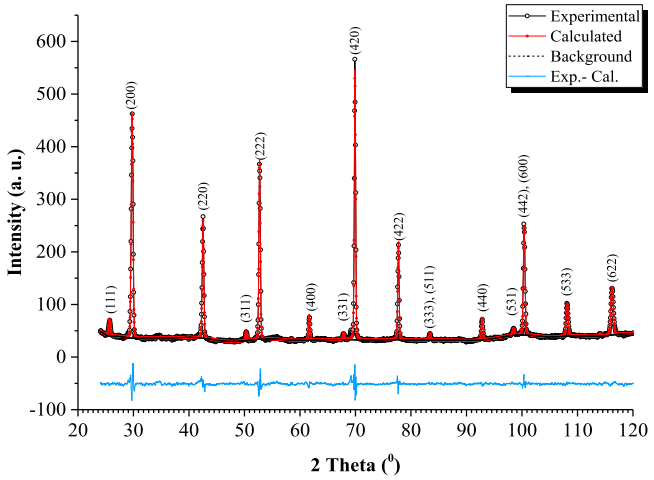

Figure 5. Refinements of the neutron diffraction data at 600 K under no applied magnetic field. The alloy is a single-phase austenite with cubic $L2_1$ crystalline structure. Similar diffraction patterns to this one (at 600 K) were also observed at 450 and 400 K.

(which is in the second region) is given in the figure 6. At this tempereture, the austenitic phase still dominates the diffraction pattern and the contribution from the 8 M modulated phase is minimal. However, there is a significant contribution from the 6 M modulated martensitic phase. At 270 K the weight fraction of the 8 M phase is less than 15% and it increases with further decrease in temperature. The martensitic transition temperature (T_M), defined as the temperature at which phase fraction of the austenite (or martensite) is 50%, is approximately 295 K.

In the final region (i.e. from 270 down to 50 K), two martensitic phases with 6 and 8 M modulations coexist. Here, the weight fraction of the 6 M phase decreases with decreasing temperature (6 M is the dominant martensitic phase just below the transition temperature). The decrease in the 6 M phase is compensated by an increase in the fraction of

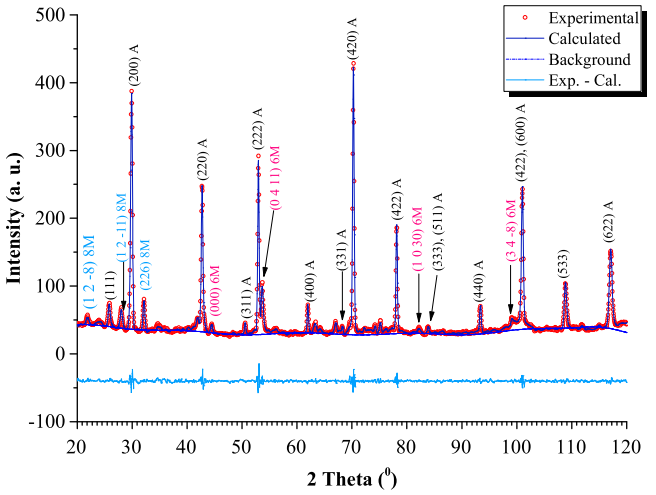

Figure 6. Refinements of the neutron diffraction data at 300 K, under no applied magnetic field. Under these conditions, the alloy is a mixture of austenitic and martensitic phases. However, the martensitic contribution is small. The hkl values of the Bragg peaks of the austenitic (A), 6, and 8 M martensitic phases are shown in black, red and blue colors, respectively.

the 8 M martensite. At 50 K, the fractional ratio of the 8 M to the 6 M phases is about 60% to 40%. We suggest that this behavior of the martensite results from the entropy of the structures; the highly ordered 8 M phase is energetically favorable at low temperatures because of its lower entropy compared to 6 M modulation.

3.4. Magnetic states and thermal hysteresis of magnetic phase transitions

Figure 7 demonstrates the behavior of the mass magnetization as a function of the temperature (in the range from 100 to 400 K) in ZFC (heating), FC (cooling), and FC (heating) routines under four different applied magnetic fields (0.005, 1, 2, and 3 T). All these thermomagnetic curves demonstrate a sharp change in the magnetization around 260 K upon cooling and 300 K upon heating of the alloy. Under all three magnetic fields, there is a higher magnetization in temperatures approximately above 270 K (upon cooling) and 310 K (upon heating) of the alloy. This indicates a ferromagnetic ordering in the austenitic phase and very weak magnetization in the martensitic phase. The weak magnetization in the martensitic phase is almost constant below some temperature in the martensitic phase. The behavior of the thermomagnetization curve in the martensitic phase could be due to a weak magnetic state such as antiferromagnetic or spin-glass.

The characteristic temperatures of the magnetic phase transition were defined by extrapolation of the linear parts of the thermomagnetic curves (figure 7). The characteristic temperatures of the pure magnetic phase transition; ferromagnetic start (FM_S), ferromagnetic finish (FM_F), lower magnetic state start (LM_S), and lower magnetic state finish (LM_F) of the thermo-magnetic curve under 3 T field, are shown in the figure 7. Additionally, two characteristic temperatures $T_{h(50)}$ and $T_{c(50)}$, were defined. Here, $T_{h(50)}$ is the

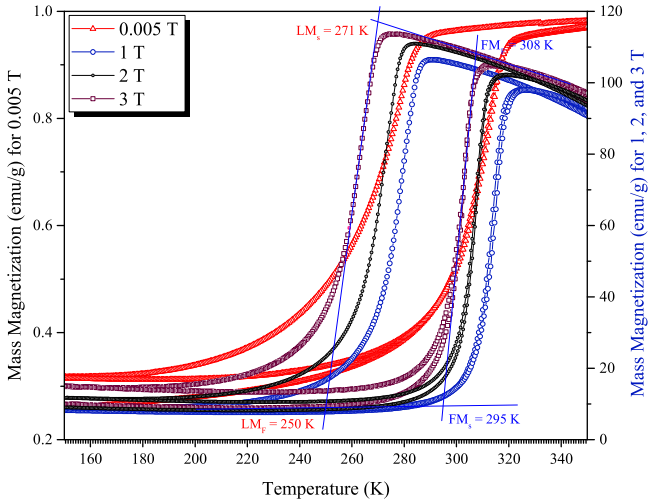

Figure 7. Thermo-magnetization curves under different magnetic fields (0.005, 1, 2 and 3 T). The characteristic temperatures of the magnetic phase transition (associated with crystallographic phase transition) were determined by extrapolating the linear parts of the thermomagnetic curves. The characteristic temperatures of the magnetic phase transition under 3 T field is given in the diagram. Magnetic phase transition temperatures decrease with increasing field.

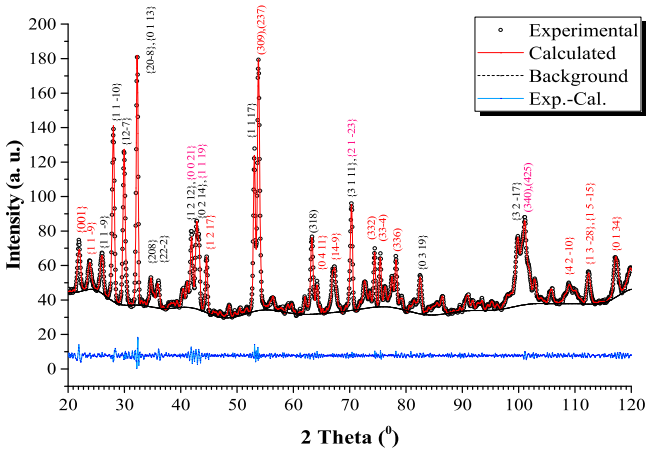

Figure 8. Rietveld refinements of neutron diffraction data collected at 250 K. At this temperature alloy is a mix of two martensitic phases: 6 and 8 M martensite. The numbers marked in black and red are the (hkl) values of the peaks of 6 M and 8 M modulated phases, respectively. There is a good agreement between experimental and calculated diffraction patterns based on mixture of modulated martensitic phases.

temperature at which the magnetization of the alloy is equal to the average value in the FC heating path, while, $T_{c(50)}$ is the temperature at which the magnetization of the alloy is equal to the average value in the FC cooling path. All the characteristic transition temperatures are listed in table 4. The hystereses associated with the magnetic phase transitions were calculated by taking the difference between $T_{h(50)}$ and $T_{c(50)}$. The magnetic phase transition temperature goes down with the increasing magnetic field. However, the associated thermal hysteresis of the magnetic phase transition goes up with increasing field.

To investigate the magnetic state of the martensitic phase further, the neutron diffraction data at low temperatures (below 250 K) were analyzed in detail. Three of the constituent atoms of this alloy (Mn, Co and Ni) have magnetic moments that interact with neutrons. If there is antiferromagnetic ordering present in the martensitic phase, there will be additional magnetic Bragg peaks, separated from crystalline peaks due to an enlargement of the magnetic unit cell compared to the crystalline unit cell [26]. Refinement of the neutron diffraction data (figure 8) collected below martensitic phase transition temperature, assuming crystallographic peaks only, is in agreement with the experimental data. No extra peaks, which could belong to antiferromagnetic ordering, were observed. This excludes antiferromagnetic ordering in the low magnetization martensitic phase.

Thermomagnetic measurements, under all four magnetic fields, exhibit a very low magnetization in the martensitic phase. Even though, the possibility of antiferromagnetic ordering in the martensitic phase is excluded, there are no sufficient evidences to confirm the magnetic nature of the martensitic phase, just below the phase transition as a spin-glass disorder. In order to investigate the magnetic nature of the alloy at very low temperatures (below 100 K), another set of DC SQUID magnetization measurements of this alloy sample were carried out in the temperature range from ~1.9 to 100 K. The experimental procedure of these measurements followed Chamberlin *et al* [27]. Under both magnetic fields, 0.05 and 0.01 T, a cusp-like maxima were observed in the mass magnetization in the FC heating path. In addition, there is a splitting between FC heating and FC cooling thermomagnetic curves (figure 9). These features indicate a spin-glass like magnetic nature of this alloy at very low temperatures [27]. From these thermo-magnetization curves, the glass transition temperature was identified to be ~19 K.

All the Co atoms reside in the regular Ni-sites (see figure 10); Mn atoms are present in all three sites with different proportions. More than 90% of the Ni atoms occupy Ni-sites and the rest in Mn-sites. Mn atoms, which carry the

Table 4. The characteristic temperatures of the magnetic phase transition associated with crystalline phase transitions.

	Characteristic temperatures (K)						
Magnetic field (T)	FM_{start}	FM_{finish}	[a]LM_{start}	[a]LM_{finish}	$T_{c\ (50)}$	$T_{h(50)}$	Thermal hysteresis (K)
1	308 ± 0.5	320 ± 0.5	287 ± 0.5	267 ± 0.5	278 ± 0.5	314 ± .05	36.0 ± 0.5
2	300 ± 0.5	313 ± 0.5	279 ± 0.5	259 ± 0.5	270 ± 0.5	308 ± 0.5	38.0 ± 0.5
3	295 ± 0.5	308 ± 0.5	271 ± 0.5	250 ± 0.5	260 ± 0.5	302 ± 0.5	42.0 ± 0.5

[a] LM—low magnetic.

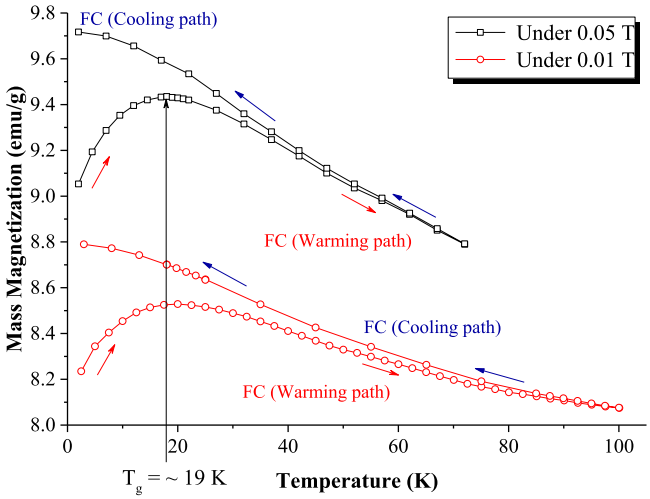

Figure 9. Thermo-magnetization curves under 0.05 and 0.10 T magnetic fields. Under both magnetic fields, a cusp like maxima are observed in the FC warming path. Additionally, there is a clear splitting between the curves under FC warming and FC cooling paths.

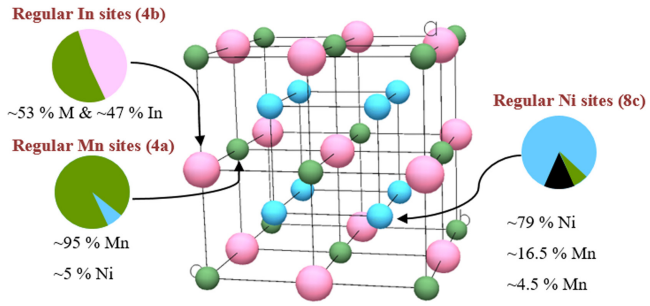

Figure 10. A schematic representation of the average site occupancies of the cubic austenitic phase.

strongest magnetic moment, occupy all possible sites in the austenitic phase. Transition to martensite will maintain the chemical order; the magnetic disorder, however, will increase due to the modulation of the martensitic structure [11]. This magnetic disorder could be the source for the observed spin-glass magnetic behavior at very low temperatures (below 20 K).

4. Conclusion

In summary, neutron diffraction studies have shown that the crystalline structure of the austenitic phase is cubic $L2_1$ ($Fm\bar{3}m$). The crystalline structure of the martensitic phase was found to be a mixture of two modulated monoclinic phases; 6 and 8 M. These modulated structures belong to the $P\,1\,2/m\,1$ space group. The site-occupancy refinements revealed that almost all the substituted Co atoms occupy the regular Ni-sites, while a small number of the Ni atoms move into the regular Mn-sites. Additionally, the majority of Mn atoms were found in the Mn-sites, while the rest reside in both In- and Ni-sites (the percentage of Mn in Ni-sites is about 5%). According to the thermomagnetic measurements, the magnetization of the martensite is very low compared to that of the austenite. Most importantly, no antiferromagnetic ordering was observed in the martensitic phase based on neutron diffraction measurements. The cusp-like maxima in the FC warming path of the thermomagnetic curves and splitting between FC warming and FC cooling curves indicate a spin-glass like magnetic nature at very low temperatures (below 20 K) in the martensitic phase. The spin-glass transition temperature was identified as 19 K under both applied fields. The modulations of the martensitic structures and disorder of the magnetic moments in the martensitic phase may be responsible for the observed spin-glass behavior.

Acknowledgments

This study was supported by award No. RUP1-7028-MO-11 of the US Civilian Research and Development Foundation (CRDF Global) and by the National Science Foundation under Cooperative Agreement No. OISE-9531011. In addition, the study was supported by the Russian Foundation for Basic Research Grant No. 13-07-12130. The authors wish to acknowledge the US National Science Foundation award number NSF-0831951. Research at Oak Ridge National Laboratory was sponsored by the Scientific User Facilities Division, Office of Basic Energy Sciences, and the US Department of Energy. Last but not least, the authors wish to acknowledge Amila Dissanayake of the Department of Physics, Western Michigan University for his help in RBS experiments.

References

[1] Ullakko K, Huang J K, Kantner C, O'Handley R C and Kokorin V V 1996 Large magnetic fieldinduced strains in Ni_2MnGa single crystals *Appl. Phys. Lett.* **69** 1966–8
[2] Krenke T, Duman E, Acet E, Wassermann E F, Moya X, Mañosa L, Planes A, Suard E and Ouladdiaf B 2007 Magnetic superelasticity and inverse magnetocaloric effect in Ni-Mn-In *Phys. Rev.* B **75** 104414
[3] Hu F, Shen B and Suna J 2000 Magnetic entropy change in $Ni_{51.5}Mn_{22.7}Ga_{25.8}$ alloy *Appl. Phys. Lett.* **76** 3460
[4] Mañosa L, González-Alonso D, Planes A, Bonnot E and Barrio M 2010 Giant solid-state barocaloric effect in the Ni–Mn–In magnetic shape-memory alloy *Nat. Mater.* **9** 478–81
[5] Liu J, Gottschall T, Skokov K P, Moore J D and Gutfleisch O 2012 Giant magnetocaloric effect driven by structural transitions *Nat. Mater.* **11** 620–6
[6] Kamantsev A *et al* 2014 Thermomagnetic and magnetocaloric properties of metamagnetic Ni-Mn-In-Co Heusler alloy in magnetic fields up to 140 kOe *Eur. Phys. J. Web Conf.* **75** 04008
[7] Kamantsev A *et al* 2015 Magnetocaloric and thermomagnetic properties of $Ni_{2.18}Mn_{0.82}Ga$ Heusler alloy in high magnetic fields up to 140 KOe *J. Appl. Phys.* **117** 163903
[8] Kainuma R, Imano Y, Ito W, Morito H, Sutou Y, Oikawa K, Fujita A, Ishida K, Okamoto S and Kitakami O 2006 Metamagnetic shape memory effect in a Heusler-type $Ni_{43}Co_7Mn_{39}Sn_{11}$ polycrystalline alloy *Appl. Phys. Lett.* **88** 192513

[9] Ito W, Nagasako M, Umetsu R Y, Kainuma R, Kanomata T and Ishida K 2008 Atomic ordering and magnetic properties in the $Ni_{45}Co_5Mn_{36.7}In_{13.3}$ metamagnetic shape memory alloy *Appl. Phys. Lett.* **93** 232503

[10] Liu J, Scheerbaum N, Hinz D and Gutfleisch O 2008 Magnetostructural transformation in Ni–Mn–In–Co ribbons *Appl. Phys. Lett.* **92** 162509

[11] Perez-Landazabal J I, Recarte V, Sanchez-Alarcos V, Gomez-Polo C and Cesari E 2013 Magnetic properties of the martensitic phase in Ni-Mn-In-Co metamagnetic *Appl. Phys. Lett.* **102** 101906

[12] Nayak A K, Suresh K G and Nigam A K 2009 Giant inverse magnetocaloric effect near room temperature in Co substituted NiMnSb Heusler alloys *J. Phys. D: Appl. Phys.* **42** 035009

[13] Priolkar K R, Bhobe P A, Lobo D, D'Souza S W, Barman S R, Chakrabarti A and Emura S 2013 Antiferromagnetic exchange interactions in $Ni_2Mn_{1.4}In_{0.6}$ ferromagnetic Heusler alloy *Phys. Rev.* B **87** 144412

[14] Umetsu R Y, Fujita A, Ito W, Kanomata T and Kainuma R 2011 Determination of the magnetic ground state in the martensite phase of Ni–Mn–Z (Z = In, Sn and Sb) off-stoichiometric Heusler alloys by nonlinear AC susceptibility *J. Phys.: Condens. Matter* **23** 326001

[15] The Van de Graaff Accelerator Facility, Deparmet of Physics, Western Michigan University [Online]. Available:(http://tesla.physics.wmich.edu/Van_de_Graaff_Accelerator_Facility/ Accessed: 29 December 2008)

[16] Mayer M 1997 SIMNRA user's guide *Technical Report IPP* Max-Planck-Institut Fur Plasmaphysik, Garching, Germany

[17] Garlea V, Chakoumakos B, Moore S, Taylor G, Chae T, Maples R, Riedel R, Lynn G and Selby D L 2010 The high-resolution powder diffractometer at the high flux isotope reactor *Appl. Phys.* A **99** 531–5

[18] Larson A and Von Dreele R 2004 General structure analysis system (GSAS) *Los Alamos National Laboratory Report LAUR* 86–748

[19] Toby B H 2001 EXPGUI, a graphical user interface for GSAS *J. Appl. Cryst.* **34** 210–3

[20] Finger L W, Kroeker M and Toby B H 2007 DRAWxtl, an open-source computer program to produce crystal-structure drawings *J. Appl. Crystallogr.* **40** 188

[21] Munter A 2013 NIST center for Neutron Research, National Institute of Standards and Technology [Online]. Available: (http://ncnr.nist.gov/resources/n-lengths/ Accessed: 01 July 2013)

[22] Bai J., Raulot J M, Zhang Y, Esling C, Zhao X and Zuo L 2011 The effects of the alloying elements Co on NiMn-Ga ferromagnetic shape memory alloys from first-principle calculations *Appl. Phys. Lett.* **98** 164103

[23] Hidnert P 1957 Thermal expansion fo some nickel alloys *J. Res. Natl Bur. Stand.* **58** 89–92

[24] Righi L, Albertini F, Villa E, Paoluzi A, Calestani G, Chernenko V, Besseghini S, Ritter C and Passaretti F 2008 Crystal structure of 7 M modulated Ni-Mn-Ga martensitic phase *Acta Mater.* **56** 4529–35

[25] Righi L, Albertini F, Fabbrici S and Paoluzi A 2011 Crystal structures of modulated martensitic phases of FSM Heusler alloys *Mater. Sci. Forum* **684** 105–16

[26] Cui J, Huang Q and Toby B H 2006 Magnetic structure refinement with neutron powder diffraction data using GSAS: a tutorial *Powder Diffr.* **21** 71

[27] Chamberlin R V, Hardiman M, Turkevich L A and Orbach R 1982 H-T phase diagram for spin-glasses: an experimental study of Ag:Mn *Phys. Rev.* B **25** 6720